



Lagrangian statistics of concentrated emulsions

Ivan Girotto^{1,2}, Andrea Scagliarini³, Roberto Benzi⁴ and Federico Toschi^{2,3,†}

¹The Abdus Salam International Centre for Theoretical Physics (ICTP) Strada Costiera, 11 - I-34151 Trieste, Italy

²Department of Applied Physics and Science Education, Eindhoven University of Technology, P.O. Box 513, 5600 MB Eindhoven, The Netherlands

³Institute for Applied Mathematics ‘Mauro Picone’ (IAC), Italian National Research Council (CNR), Via dei Taurini 19, I-00185 Rome, Italy

⁴Department of Physics and INFN, University of Rome ‘Tor Vergata’, Via della Ricerca Scientifica 1, I-00133 Rome, Italy

(Received 26 July 2023; revised 24 February 2024; accepted 8 April 2024)

The dynamics of stabilised concentrated emulsions presents a rich phenomenology including chaotic emulsification, non-Newtonian rheology and ageing dynamics at rest. Macroscopic rheology results from the complex droplet microdynamics and, in turn, droplet dynamics is influenced by macroscopic flows via the competing action of hydrodynamic and interfacial stresses, giving rise to a complex tangle of elastoplastic effects, diffusion, breakups and coalescence events. This tight multiscale coupling, together with the daunting challenge of experimentally investigating droplets under flow, has hindered the understanding of concentrated emulsions dynamics. We present results from three-dimensional numerical simulations of emulsions that resolve the shape and dynamics of individual droplets, along with the macroscopic flows. We investigate droplet dispersion statistics, measuring probability density functions (p.d.f.s) of droplet displacements and velocities, changing the concentration, in the stirred and ageing regimes. We provide the first measurements, in concentrated emulsions, of the relative droplet–droplet separations p.d.f. and of the droplet acceleration p.d.f., which becomes strongly non-Gaussian as the volume fraction is increased above the jamming point. Cooperative effects, arising when droplets are in contact, are argued to be responsible of the anomalous superdiffusive behaviour of the mean square displacement and of the pair separation at long times, in both the stirred and in the ageing regimes. This superdiffusive behaviour is reflected in a non-Gaussian pair separation p.d.f., whose analytical form is investigated, in the ageing regime, by means of theoretical arguments. This work

† Email address for correspondence: f.toschi@tue.nl

paves the way to developing a connection between Lagrangian dynamics and rheology in concentrated emulsions.

Key words: emulsions, breakup/coalescence, multiphase flow

1. Introduction

Understanding the dynamics of concentrated suspensions of soft, athermal particles such as emulsions, foams or gels is key to many natural and industrial processes (Larson 1999; Coussot 2005; McClements 2015). A central question concerns the connection between mechanisms occurring at the microstructure level and the macroscopic flow and rheological properties in these systems (Cohen-Addad, Hohler & Pitois 2013; Dollet & Christophe 2014; Bonn *et al.* 2017; Dijkstra 2019). For instance, irreversible topological rearrangements, corresponding to local yielding events, are known to be directly related to the inhomogeneous fluidisation of soft glassy materials (Goyon *et al.* 2008; Bocquet, Colin & Ajdari 2009; Bouzid *et al.* 2015; Dollet, Scagliarini & Sbragaglia 2015; Fei *et al.* 2020). Fostered by such rheological implications, but going beyond them, many experimental and numerical studies have been devoted to characterising the microdynamics of soft jammed materials by tracking individual mesoconstituents (droplets, bubbles, grains, etc.), unveiling their anomalous dispersion properties (Durian, Weitz & Pine 1991; Durian 1995; Lowenberg & Hinch 1996; Mason *et al.* 1997; Cipelletti *et al.* 2003; Ruzicka, Zulian & Ruocco 2004; Cerbino & Trappe 2008; Squires & Mason 2010). Looking at the droplet statistical dynamics from a Lagrangian viewpoint is, therefore, crucial. Highly packed emulsions/foams are typically characterised in simple flows (oscillatory Couette, Poiseuille, etc.), or even at rest, in the ageing regime (Mason & Weitz 1995; Ramos & Cipelletti 2001; Cipelletti *et al.* 2003; Cipelletti & Ramos 2005; Li, Peng & McKenna 2019; Giavazzi, Trappe & Cerbino 2021). On the other hand, Lagrangian studies of dispersions in complex, high Reynolds number flows are widely represented in the literature, but in extremely diluted conditions (Toschi & Bodenschatz 2009; Brandt & Coletti 2022). The investigation of the microdynamics of concentrated systems in complex flows, of relevance, e.g. for emulsification processes (Tcholakova *et al.* 2007; Vankova *et al.* 2007a,b), is, in fact, a formidable task due to the need to cope, at the same time, with the two-way coupling of the interfacial dynamics with the hydrodynamics and with the droplet/bubble tracking.

Motivated by the above discussion, in the present paper we aim at investigating the statistical dynamics of emulsion droplets in a systematic way across various concentrations (from semi-dilute to jammed conditions), under the action of a large-scale forcing, inducing a chaotic, turbulent-like flow, and during ageing. For our purpose, we employ a mesoscopic numerical model, developed over the last 15 years, to simulate the hydrodynamics of three-dimensional immiscible fluid mixtures, stabilised against full phase separation, equipped with a droplet tracking algorithm. The same approach was used in a recent publication (Giroto *et al.* 2022) to show how to prepare an emulsion, by means of a suitable combination of stirring and injection of the dispersed phase, and how to characterise it both structurally and rheologically: structurally, by looking at the evolution of the droplet size distribution, which we found to be in close agreement with known experimental results; rheologically, by looking at the emergence of the yield stress for large enough volume fractions, ϕ . In Giroto *et al.* (2022), we also showed that, for a given amplitude of the large-scale stirring, upon increasing the volume fraction ϕ of

the disperse phase, there exists a critical value ϕ_{cpi} at which a sudden catastrophic phase inversion occurs (Bouchama *et al.* 2003; Perazzo, Preziosi & Guido 2015) (see figure 5 in Giroto *et al.* 2022).

At low volume fractions droplets are normally far from each other and regularly collide due to the presence of the flow; elastoplastic rearrangements are not defined in this regime. For high volume fractions ($\gtrsim 60\%$), on the contrary, droplets are mostly in contact with each other and the emulsion regularly undergoes elastoplastic rearrangements; it is not possible to properly talk of collisions in this case as the droplets are always in contact. For a small range of intermediate volume fractions, one could observe both collisions and elastoplastic rearrangements; in this regime it is, however, very hard to define whether or not droplets are in contact with each other and therefore to clearly distinguish between a flow-induced collision or an elastoplastic rearrangement. Here, we provide measurements of droplet absolute (single) and relative (pair) dispersions, velocity and acceleration distributions, as well as of the droplet breakup, β , and coalescence, κ , rates. An interesting, and we feel important, result of our investigation is that β , κ and the average droplet size shows divergent-like behaviour for $\phi \rightarrow \phi_{cpi}$, which is consistent (in the language of statistical mechanics) with the identification of ϕ_{cpi} as a critical point of a phase transition. Also, upon increasing ϕ from a semi-dilute to a highly concentrated emulsion, droplet accelerations show increasingly intermittent features due to increasing stiffness and elastoplastic effects in the system. For large enough volume fraction, we also studied the so-called ageing regime, i.e. we stop the forcing and we look at the droplet dynamics. Remarkably, droplet dispersion and pair separation (here studied for the first time) show a ballistic regime followed by a clear superdiffusive behaviour. For pair dispersion in the ageing regime we propose theoretical models that show good agreement with the measurements.

The paper is organised as follows. In §2 we present the numerical method and we provide an extensive introduction to the tracking algorithm. The main results are reported in §3, organised in subsections relative to the stirred and ageing regimes. Conclusions and perspectives are drawn in §4.

2. Methods

2.1. Multicomponent emulsion modelling

The emulsion is described in terms of the density fields of the two components, conventionally indicated as O and W (for, e.g. ‘oil’ and ‘water’), $\rho_{O,W}$, and the incompressible barycentric fluid velocity field, \mathbf{u} , which evolve according to the following equations:

$$\left. \begin{aligned} \partial_t \rho_\sigma + \nabla \cdot (\rho_\sigma \mathbf{u}) &= 0 \quad \sigma = O, W \\ \rho_f (\partial_t \mathbf{u} + \mathbf{u} \cdot \nabla \mathbf{u}) &= -\nabla p + \nabla \cdot \mathbf{P}^{(mix)} + \eta \nabla^2 \mathbf{u} + \mathbf{F}^{(ext)}, \end{aligned} \right\} \quad (2.1)$$

where $\rho_f = \rho_O + \rho_W$ is the total density, p is the pressure, η is the dynamic viscosity and $\mathbf{F}^{(ext)}$ a forcing term; $\mathbf{P}_{ij}^{(mix)}[\rho_O, \rho_W, \partial_i \rho_O, \partial_i \rho_W, \dots]$, a function of the two density fields and of their derivatives, is the non-ideal contribution to the pressure tensor. Equations (2.1) are integrated numerically on a three-dimensional (3-D) cubic domain of size L^3 with periodic boundary conditions by means of a two-component lattice Boltzmann method (Benzi, Succi & Vergassola 1992) in the Shan–Chen formulation (Shan & Chen 1993, 1994). The lattice Boltzmann equation for the discrete probability distribution

functions, $f_{\sigma l}$, reads (the time step is set to unity, $\Delta = 1$)

$$f_{\sigma l}(\mathbf{x} + \mathbf{e}_l, t + 1) - f_{\sigma l}(\mathbf{x}, t) = -\frac{1}{\tau_\sigma} (f_{\sigma l}(\mathbf{x}, t) - f_{\sigma l}^{eq}(\mathbf{x}, t)) + S_{\sigma l}^{(tot)}(\mathbf{x}, t), \quad (2.2)$$

where the index l runs over the discrete set of $Q = 19$ 3-D lattice velocities ($D3Q19$ model) $\{\mathbf{e}_l\}$ ($l = 0, 1, \dots, 18$), and σ labels each of the two immiscible fluids (hereafter, we take the same relaxation time for the two species, i.e. $\tau_O = \tau_W \equiv \tau$). The equilibrium distribution function is given by the usual polynomial expansion of the Maxwell–Boltzmann distribution, valid in the limit of small fluid velocity, namely

$$f_{\sigma l}^{eq}(\mathbf{x}, t) = \rho_\sigma \omega_l \left(1 + \frac{\mathbf{e}_l \cdot \mathbf{u}}{c_s^2} + \frac{(\mathbf{e}_l \cdot \mathbf{u})^2}{2c_s^4} - \frac{\mathbf{u} \cdot \mathbf{u}}{2c_s^2} \right), \quad (2.3)$$

with ω_l being the usual set of suitably chosen weights so as to maximise the algebraic degree of precision in the computation of the hydrodynamic fields and $c_s = 1/\sqrt{3}$ a characteristic molecular velocity (a constant of the model). The hydrodynamical fields can be calculated from the lattice probability density functions $f_{\sigma l}$ as $\rho_\sigma = \sum_l f_{\sigma l}$ and $\rho \mathbf{u} = \sum_{\sigma l} f_{\sigma l} \mathbf{e}_l$ (where $\rho = \sum_\sigma \rho_\sigma$ is the total density of the fluid). The source term $S_{\sigma l}^{(tot)} = \omega_l \mathbf{e}_l \cdot \mathbf{F}_\sigma^{(tot)} / c_s^2$ stems from all the forces (internal and external) acting in the system, $\mathbf{F}_\sigma^{(tot)} = \mathbf{F}_\sigma + \mathbf{F}_\sigma^{(ext)}$. In particular, \mathbf{F}_σ , incorporates the two kinds of lattice interaction forces, $\mathbf{F}_\sigma = \mathbf{F}_\sigma^{(r)} + \mathbf{F}_\sigma^{(f)}$ and $\mathbf{F}_\sigma^{(r)}$ is the standard Shan–Chen inter-species repulsion of amplitude $G_{OW} > 0$, which is responsible of phase separation, and reads

$$\mathbf{F}_\sigma^{(r)}(\mathbf{x}, t) = -G_{OW} \rho_\sigma(\mathbf{x}, t) \sum_{l, \bar{\sigma} \neq \sigma} \omega_l \rho_{\bar{\sigma}}(\mathbf{x} + \mathbf{e}_l, t) \mathbf{e}_l. \quad (2.4)$$

The second term, $\mathbf{F}_\sigma^{(f)}$, consists of a short-range intra-species attraction, involving only nearest-neighbour sites (\mathcal{I}_1), and a long-range self-repulsion, extended up to next-to-nearest neighbours (\mathcal{I}_2) (Benzi *et al.* 2009), namely

$$\begin{aligned} \mathbf{F}_\sigma^{(f)}(\mathbf{r}, t) = & -G_{\sigma\sigma,1} \rho_\sigma(\mathbf{x}, t) \sum_{l \in \mathcal{I}_1} \omega_l \rho_\sigma(\mathbf{x} + \mathbf{e}_l, t) \mathbf{e}_l \\ & - G_{\sigma\sigma,2} \rho_\sigma(\mathbf{x}, t) \sum_{l \in \mathcal{I}_1 \cup \mathcal{I}_2} p_l \rho_\sigma(\mathbf{x} + \mathbf{e}_l, t) \mathbf{e}_l, \end{aligned} \quad (2.5)$$

where $G_{OO,1}, G_{WW,1} < 0$ and $G_{OO,2}, G_{WW,2} > 0$ are interaction parameters and p_l are the weights of the $D3Q125$ model. This type of repulsive interaction $G_{\sigma\sigma,2}$ represents a mesoscopic phenomenological modelling of surfactants and provides a mechanism of stabilisation against coalescence of close-to-contact droplets (the superscript ‘ f ’ stands in fact for ‘frustration’), promoting the emergence of a positive disjoining pressure, $\Pi > 0$, within the liquid film separating the approaching interfaces (Benzi *et al.* 2009, 2010, 2014).

The above method, in the small Mach, $Ma \sim u/c_s$ (where u is a typical velocity, e.g. the root mean square), and Knudsen, $Kn \sim \Delta x/L$, limits, works as a numerical solver (second-order accurate in space and time Krüger *et al.* 2016; Succi 2018) for (2.1), with $p = c_s^2 \rho_f$ and $\eta = \rho_f c_s^2 (\tau - 1/2)$. The bridge between this mesoscopic lattice interaction model and the thermodynamic and physico-chemical properties (such as equation of state, surface tension and disjoining pressure) of the mixture can be realised in terms of the mechanical equilibrium condition relating the interaction force and the non-ideal

part of the stress tensor, $\mathbf{P}^{(mix)}$ (Sbragaglia *et al.* 2012; Belardinelli & Sbragaglia 2013). The surface tension, Γ , is computed from its mechanical definition as the integral of the mismatch between the normal and tangential components of $\mathbf{P}^{(mix)}$ across a flat interface at equilibrium, i.e. considering without loss of generality a two-dimensional problem, $\Gamma = \int_{-\infty}^{+\infty} (P_{xx}^{(mix)} - P_{yy}^{(mix)})(x) dx$ (Rowlinson & Widom 2002). Analogously, the disjoining pressure, Π , can be determined measuring the overall film tension, Γ_f , as the integral of the normal–transverse stress tensor mismatch across two flat interfaces separated by a liquid layer of width h . The disjoining pressure is related to Γ_f as $h(d\Pi/dh) = d\Gamma_f(h)/dh$ (Bergeron 1999; Sbragaglia *et al.* 2012). The range of interaction between opposing interfaces dictated by such disjoining pressure, for a suitable choice of the lattice interaction parameters, is of the order of a few lattice spacings (typically ~ 5). The large-scale forcing needed to generate the chaotic stirring that mixes the two fluids, $\mathbf{F}^{(ext)}$, takes the following form:

$$F_i^{(ext)}(\mathbf{x}, t) = \sum_{\sigma} F_{\sigma i}^{(ext)}(\mathbf{x}, t) = A \sum_{\sigma} \rho_{\sigma} \sum_{k \leq 2\pi\sqrt{2}/Lj \neq i} \sum \left[\sin(k_j x_j + \Phi_j^{(k)}(t)) \right], \quad (2.6)$$

where $i, j = 1, 2, 3$, A is the forcing amplitude, \mathbf{k} is the wavevector and the sum is limited to $k^2 = k_1^2 + k_2^2 + k_3^2 \leq 8\pi/L$. The phases $\Phi_j^{(k)}$ are evolved in time according to independent Ornstein–Uhlenbeck processes with the same relaxation times $T = L/u_{rms}$, where L is the cubic box edge and u_{rms} is the root mean squared velocity (Biferale *et al.* 2011; Perlekar *et al.* 2012). The code has been extensively used and validated in the past by several groups to study: droplet deformation and breakup (Gupta, Sbragaglia & Scagliarini 2015), also in association with thermocapillary (Gupta *et al.* 2016) and viscoelastic (Gupta & Sbragaglia 2016) effects; droplet formation in microfluidic devices (Chiarello *et al.* 2017); sliding droplets (Varagnolo *et al.* 2015); droplet breakup in turbulent flows (Perlekar *et al.* 2012); spinodal decomposition arrest in turbulent flows (Perlekar *et al.* 2014), among others.

2.2. Droplet tracking

We present now the tracking algorithm and discuss its implementation. The algorithm combines (i) the process of identification of all droplets constituting the emulsion at two different and consecutive time steps (hereafter called labelling), with (ii) a stage describing the kinematics of each droplet (the actual tracking).

In the labelling step, individual droplets, defined as connected clusters of lattice points such that the local density exceeds a prescribed threshold (equal to $\rho_O^{(max)} - \rho_O^{(min)}$), are identified by means of the Hoshen–Kopelman algorithm (Hoshen & Kopelman 1976; Frijters, Krüger & Harting 2015). This approach echoes what is known in the image processing jargon as connected component labelling (He *et al.* 2017); similar techniques have been recently applied to multiphase fluid dynamics in volume of fluid simulations (Herrmann 2010; Hendrickson, Weymouth & Yue 2020).

The tracking is based on the computation of the probability of obtaining volume transfer among droplets in space and time as described in Gaylo, Hendrickson & Yue (2022), Gao *et al.* (2021) and Chan *et al.* (2021). This is performed as follows. Let us suppose that, in the domain, at time t_1 , there are N_1 droplets and at a later dump $t_2 = t_1 + \Delta t$ there are N_2 droplets. We define a set of droplet indicator fields $\rho_k(x, t)$ (with k running over the all droplets), which are equal to k if, at time t , x is inside the k droplet, and are equal to 0 elsewhere. In the following, the ‘state’ representing the droplet will be denoted in the ket notation (reminiscent of quantum mechanics states) as $|k, t\rangle$ (the state is assumed to be

normalised by square root of the droplet volume, $\sqrt{V_k}$, such that the transition probability for a droplet k_1 at a time t_1 to end up in a droplet k_2 at a time t_2 is given by the bra-ket expression

$$P_{k_1 \rightarrow k_2} = \langle k_2, t_2 | k_1, t_1 \rangle = \frac{1}{V} \int \rho_{k_2}(\mathbf{x}, t_2) \rho_{k_1}(\mathbf{x}, t_1) d\mathbf{x}, \quad V = \sqrt{V_{k_1} V_{k_2}}. \quad (2.7a,b)$$

This transition probability is equal to 1 in the case that droplets k_1 and k_2 perfectly overlap and it is zero if they do not overlap at all. A high P value gives us, therefore, the confidence in having re-identified the same droplet at two different time steps. What happens if a droplet is not deforming and just translating with uniform velocity \mathbf{v} ? We expect that the probability will decrease due to an imperfect overlap between the droplet k at time t and the same droplet k , displaced by $\mathbf{v}\Delta t$ at time $t + \Delta t$, where \mathbf{v} is the average velocity of all grid points included in a droplet. Therefore, we expect that the maximal correlation will occur for

$$\langle k, t + \Delta t | k, t \rangle = \frac{1}{V} \int \rho_k(\mathbf{x} + \mathbf{v}\Delta t, t) \rho_k(\mathbf{x}, t + \Delta t) d\mathbf{x}. \quad (2.8)$$

Of course, the size of this effect is proportional to Δt . In order to reduce the effect of the translation of the droplet k at a given Δt we implement a Kalman filter, evaluating the overlap against that predicted at the same $t + \Delta t$, shifting the initial position at time t forwards by $\mathbf{v}\Delta t$. For all the data shown, the tracking is implemented with $\Delta t = 100$ lattice Boltzmann time steps.

3. Results

In this section, we provide results aimed at characterising the dynamics of individual droplets (e.g. their velocities and accelerations, as well as the absolute and relative dispersions), on changing the volume fraction of the dispersed phase from $\phi = 38\%$ to $\phi = 77\%$. All simulations were performed on a cubic grid of side $L = 512$ lattice points, the kinematic viscosity was $\nu = 1/6$ for both components, (in lattice Boltzmann units; hereafter, dimensional quantities will be all expressed in such units) and the total density $\rho_f = 1.36$ (giving a dynamic viscosity $\eta = \rho_f \nu \approx 0.23$). With reference to [figure 1](#), where we plot the temporal variation of the number density of droplets N_D/L^3 , we give first a cursory description of the emulsification process, indicated as phase (I) in the figure (further details can be found in [Girotto et al. 2022](#)). All simulations are run for a total of 9×10^6 time steps. Starting from an initial condition with $\phi = 30\%$, where the two components are fully separated by a flat interface, the emulsion is created applying the large-scale stirring force, (2.6), with magnitude $A = 4.85 \times 10^{-7}$, while injecting the dispersed phase until the desired value is reached. The duration of the injection phase, t_{inj} , depends, then, on the target volume fraction (see [table 1](#)). The forcing is applied up to $t_F = 3 \times 10^6$. The evolution of the system is then monitored for a further 6×10^6 time steps. The tracking algorithm is activated at $t_0 = 1.25 \times 10^6$; for what we call, hereafter, the stirred regime (phase (II) in [figure 1](#)) we collect statistics over the interval $t \in [t_0, t_F]$ (which is statistically stationary, as can be appreciated from the figure of $N_D(t)$, but also looking at other observables, such as the mean square velocity), whereas, for the ageing regime (phase (III) in [figure 1](#)), we consider data in the interval $t \in [t_A^{(i)}, t_A^{(f)}]$, with $t_A^{(i)} = 7 \times 10^6$ and $t_A^{(f)} = 9 \times 10^6$, (the intermediate relaxation phase, $t \in [t_F, t_A^{(i)}]$, is not shown in [figure 1](#), for the sake of clarity of visualisation). In [figure 2](#) we show snapshots of

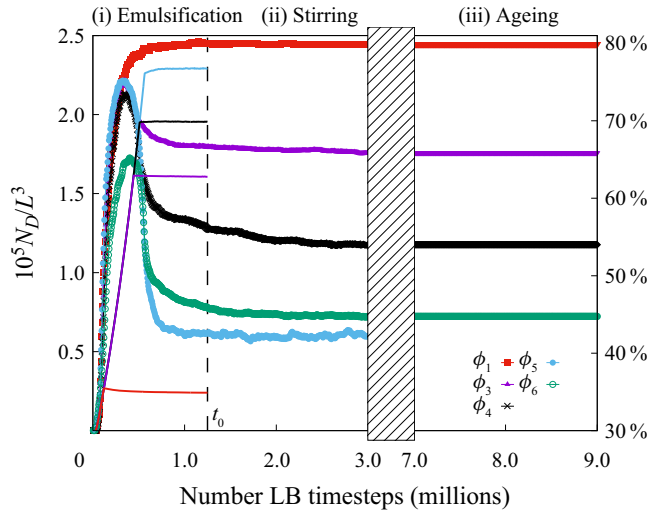


Figure 1. Number density of droplets, N_D/L^3 , as a function of time for a set of four simulations, labelled with the corresponding target (steady state) volume fractions (ϕ) of the dispersed phase (see table 1 for further details). The solid lines (colour coded for the droplet number density) indicate the time evolution of the volume fraction during emulsification. The vertical dashed line highlights the starting time of tracking, $t_0 = 1.25 \times 10^6$. All simulations are stirred with the same forcing amplitude parameter ($A = 4.85 \times 10^{-7}$, see (2.6)), except for the case indicated with hollow circles ($A = 4.05 \times 10^{-7}$, run labelled as ϕ_6 in table 1). The relaxation phase $t \in [t_F, t_A^{(i)}]$ is omitted for the sake of clarity of visualisation.

the morphology of the emulsions at $t = t_F$, for different volume fractions. Semi-dilute emulsions present a high number of small spherical droplets, whereas concentrated emulsions are constituted of a smaller number of non-spherical larger droplets. We report in table 1 the mean and root mean square (r.m.s.) values of some relevant observables (averaged in space and in time over the stirred phase, $t \in [t_0, t_F]$, and over the ageing phase, $t \in [7 \times 10^6, 9 \times 10^6]$, respectively), for the various volume fractions considered. One can immediately notice that, on increasing the volume fraction, accelerations and velocities r.m.s. decrease, implying a higher effective viscosity, while at the same time, the trend of the r.m.s. droplet diameter, d_{rms} , shows an increase in polydispersity.

Figure 3 shows the mean rates of breakup ($\bar{\beta}$) and coalescence ($\bar{\kappa}$), i.e. the number of events per unit time, averaged over the stirred regime as a function of the volume fraction ϕ (in the inset we report $\beta(t)$ and $\kappa(t)$ as a function of time for $\phi = 70\%$, 77%). In the steady state, the system is in a dynamical equilibrium with $N_D(t)$ essentially constant (see figure 1), therefore the breakup and coalescence rates approximately balance each other, $\beta(t) \approx \kappa(t)$; moreover, both mean rates are extremely low ($\sim 10^{-3}$) for $\phi < \phi_c = 64\%$, i.e. below jamming (in this regime, in particular for the lowest volume fraction considered, we detect very few events, which makes the statistical error relatively high and justifies the discrepancy between $\bar{\beta}$ and $\bar{\kappa}$), whereas they increase steeply with ϕ for $\phi > \phi_c$. Interestingly, ϕ_c is in the expected range of volume fractions for random close packing of spheres in three dimensions (Torquato & Stillinger 2010). The growth of $\bar{\beta}$ and $\bar{\kappa}$ above ϕ_c is particularly steep, suggesting a divergent behaviour as the volume fraction approaches a ‘critical’ value which can be arguably identified with the occurrence of the catastrophic phase inversion, ϕ_{cpi} . A further hint to a critical phenomenon is given in the insets where

ϕ	ϕ	t_{inj}	$\overline{ND}^{(s)}$	$U_{rms}^{(s)}$	$a_{rms}^{(s)}$	$T_L^{(s)}$	(d)	d_{rms}	t_G	$U_{rms}^{(a)}$	$a_{rms}^{(a)}$	$T_L^{(a)}$
$\phi_1 = 38\%$	$\phi_1 = 38\%$	1.5×10^5	3300	2.8×10^{-2}	4.6×10^{-4}	1.8×10^4	30	4	180	2.0×10^{-5}	1.2×10^{-7}	2.6×10^7
$\phi_2 = 49\%$	$\phi_2 = 49\%$	3×10^5	3100	2.5×10^{-2}	3.6×10^{-4}	2.0×10^4	34	5	97	1.7×10^{-5}	7.7×10^{-8}	3.0×10^7
$\phi_3 = 64\%$	$\phi_3 = 64\%$	4.6×10^5	2400	2.0×10^{-2}	2.6×10^{-4}	2.6×10^4	40	6	8	5.1×10^{-5}	2.6×10^{-7}	10^7
$\phi_4 = 70\%$	$\phi_4 = 70\%$	5.2×10^5	1600	1.8×10^{-2}	2.2×10^{-4}	2.8×10^4	48	8	1.1	6.0×10^{-5}	4.2×10^{-7}	8.5×10^6
$\phi_5 = 77\%$	$\phi_5 = 77\%$	5.8×10^5	800	1.7×10^{-2}	2.1×10^{-4}	3.0×10^4	60	17	0.1	—	—	—
$\phi_6 = 77\%$	$\phi_6 = 77\%$	5.8×10^5	970	—	—	—	58	12	—	7.0×10^{-5}	6.7×10^{-7}	7.3×10^6

Table 1. Relevant averaged quantities from the simulations at the different volume fractions ϕ . The overline, $\bar{()}$, indicates time average, the brackets, $(())$, indicate an average over time and over the ensemble of droplets. The superscripts (s, a) indicate that the averages have been taken over the statistically steady stirring regime ($t \in [t_0, t_F]$) and over the ageing regime ($t \in [7 \times 10^6, 9 \times 10^6]$), respectively. The various columns contain: t_{inj} , injection endtime; $\overline{ND}^{(s)}$, mean droplet number (stirring); $U_{rms}^{(s)}$, r.m.s. droplet velocity (stirring); $a_{rms}^{(s)}$, r.m.s. droplet acceleration (stirring); $T_L^{(s)} = L/U_{rms}^{(s)}$, large eddy turnover time (stirring); d_{rms} , mean droplet diameter; d_{rms} , standard deviation of the droplet diameter; t_G , mean (dimensionless) droplet life time; $U_{rms}^{(a)}$, r.m.s. droplet velocity (ageing); $a_{rms}^{(a)}$, r.m.s. droplet acceleration (ageing); $T_L^{(a)} = L/U_{rms}^{(a)}$, large eddy turnover time (ageing). Numerical values of the simulations parameters are: kinematic viscosity, $\nu = 1/6$; total fluid density, $\rho_f = 1.36$; surface tension, $\Gamma = 0.0238$ (correspondingly, the capillary number, based on the r.m.s. velocity, $Ca = \eta U_{rms}/\Gamma$, ranges between $Ca = 0.16$ and $Ca = 0.27$, for the highest and lowest volume fractions, respectively); forcing amplitude, $A = 4.85 \times 10^{-7}$ (except for the run ϕ_6 for which $A = 4.05 \times 10^{-7}$); simulation box side, $L = 512$.

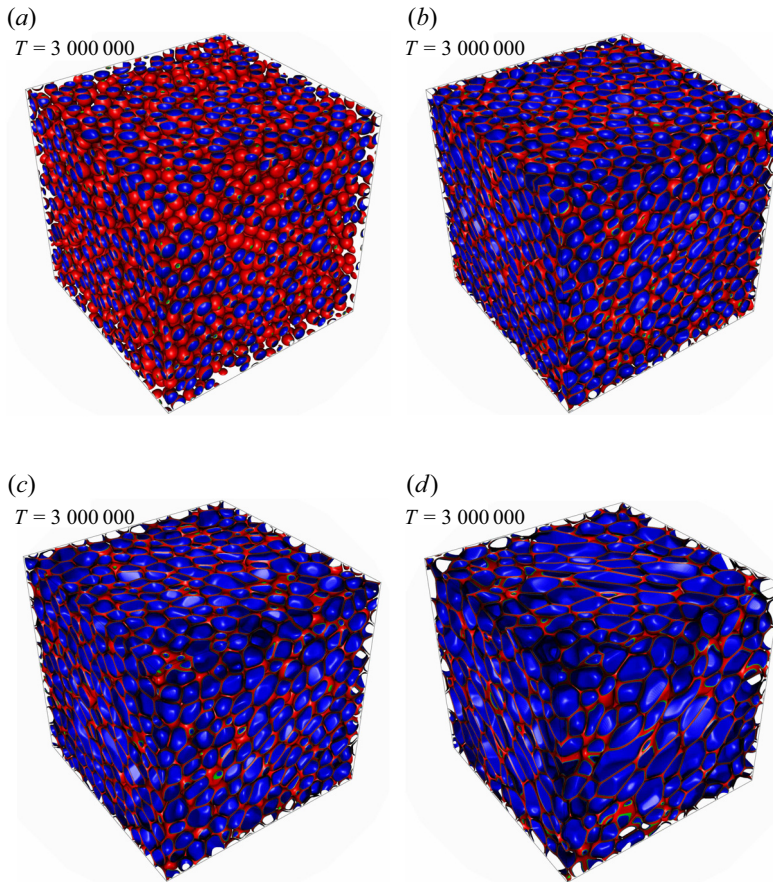


Figure 2. Snapshots from the stirred regime showing the morphology of the emulsions. On increasing the volume fraction, ϕ , a lower number of larger droplets are observed. Volume fractions below $\phi_c = 64\%$ (a value compatible with the random close packing of spheres in three dimensions) are characterised by spherical droplets, whereas higher fractions ($\phi > \phi_c$) clearly show highly deformed droplets. More quantitative details can be found in [table 1](#). Panels show (a) $\phi = 38\%$, (b) $\phi = 64\%$, (c) $\phi = 70\%$, (d) $\phi = 77\%$.

$\bar{\beta}$, $\bar{\kappa}$ (bottom) and the mean droplet diameter $\langle d \rangle$ (top) are shown in doubly logarithmic plots vs $\phi_{cpi} - \phi$, highlighting the power-law character of the divergence.

The number of breakup and coalescence events depends, of course, on the intensity of the hydrodynamic stresses involved. To see how these quantities can give a flavour of the stability of the emulsion to the applied forcing, let us introduce an average droplet life time, $t_G = N_D U_{rms} / \beta L$, non-dimensionalised by the large eddy turnover time; from [table 1](#), we see that, below jamming ($\phi \leq \phi_c$) $t_G \gg 1$, i.e. the droplets, on average, tend to preserve their integrity during the whole simulation, whereas, in the densely packed systems ($\phi > \phi_c$), t_G abruptly drops (down to $t_G \approx 0.1$ for the largest volume fraction, $\phi = 77\%$).

3.1. Velocity and acceleration statistics: stirred regime

In [figure 4](#) we report the p.d.f.s of the droplet velocities for volume fractions $\phi = 38\%$, $\phi = 64\%$ and $\phi = 77\%$. In both cases the p.d.f.s show a bell shape, but in a range of intermediate values of velocities $|v|$ they develop regions with non-monotonic curvature,

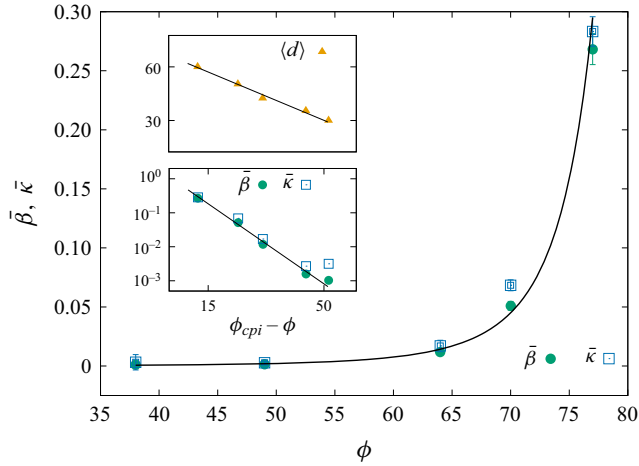


Figure 3. (Main panel). Mean breakup ($\bar{\beta}$) and coalescence ($\bar{\kappa}$) rates (averaged over stirred regime) as a function of the volume fraction concentration ϕ . The rates equal each other, consistently with the dynamical equilibrium observed at steady state; both rates are very low ($\sim 10^{-3}$) and basically insensitive to the volume fraction below jamming ($\phi_c \approx 64\%$) and above it they increase steeply with ϕ . The solid line represents the function $g(\phi) = C/(\phi_{cpi} - \phi)^q$, which is telling us that the mean breakup and coalescence rates tend to diverge as the volume fraction approaches a critical value ϕ_{cpi} , identifiable with that of catastrophic phase inversion (whence the subscript); fitting values of the parameters are $\phi_{cpi} = 90.5\%$, $q = 4.5$ and $C \approx 3.6 \times 10^4$. (Bottom inset) Log–log plot of the mean breakup and coalescence rates as function of the distance from ϕ_{cpi} ; the solid line is the function $g(\phi)$. (Top inset) Mean droplet diameter as a function of $\phi_{cpi} - \phi$; the solid line is a power-law fit with exponent -0.52 .

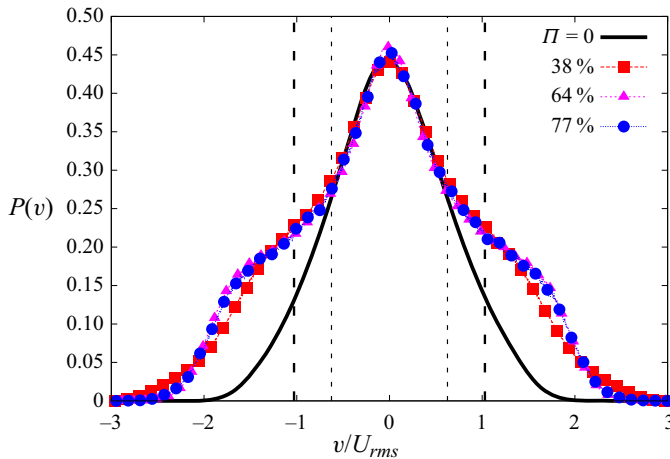


Figure 4. Probability density functions (p.d.f.s) of the droplet velocities (in units of their respective r.m.s. values), for $\phi = 38\%$, $\phi = 64\%$ and $\phi = 77\%$, computed over the forced steady state. In all cases the curves show two marked inflection points, around $v \approx \pm v_c = 0.0175$ (indicated with vertical dashed lines for $\phi = 38\%$, thin line, and $\phi = 77\%$, thick line), which are, instead, suppressed when the disjoining pressure is deactivated, $\Pi = 0$ (solid line).

which are more pronounced in the concentrated case. We ascribe such a peculiar shape to the droplet–droplet interactions (collisions and/or elastoplastic deformations). The characteristic velocity v_c can be then estimated from the balance of the elastic force and the Stokesian drag for a spherical droplet of diameter d , $F_S = 3\pi\eta d v_c$. The elastic force acting on droplets squeezed against each other is due to the disjoining pressure Π

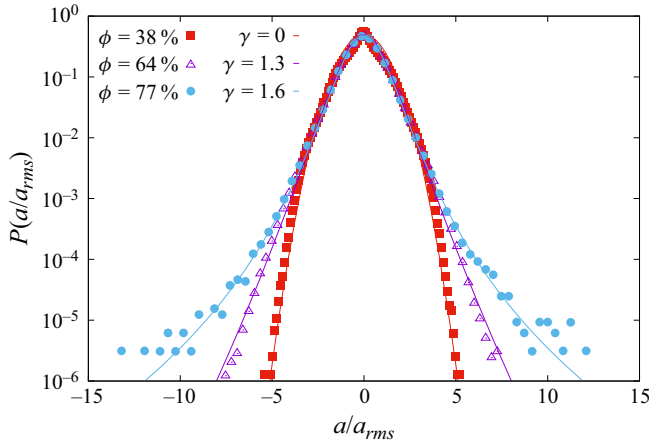


Figure 5. The p.d.f.s of the droplet accelerations, for $\phi = 38\%$, 64% , 77% , computed over the statistically steady forced state. The p.d.f.s are normalised to have unitary area. The values of a_{rms} are given in table 1. The solid lines are fits from (3.1) with $\sigma = 1$ and $\beta = 0.35$, whereby the non-Gaussianity parameter γ takes the values $\gamma = 0$ (corresponding to the Gaussian distribution) for $\phi = 38\%$, $\gamma = 1.32$ for $\phi = 64\%$ and $\gamma = 1.6$ for $\phi = 77\%$.

stabilising the inter-droplet thin film; at mechanical equilibrium the disjoining pressure equals the capillary pressure at the curved droplet interface (Derjaguin & Churaev 1978), therefore, the force can be estimated as the Laplace pressure times the cross-sectional area, $F_{el} \sim (2\Gamma/d)\pi(d/2)^2$, where Γ is the surface tension. Letting $F_{el} \sim F_S$ gives $v_c \sim \Gamma/6\eta = 0.0175$; from figure 4 we see that, indeed, the inflections are located around $v \sim \pm v_c$. To test our conjecture further, we have run a simulation setting the competing lattice interactions responsible for the emergence of the disjoining pressure to zero ($G_{00,1} = G_{WW,1} = G_{00,2} = G_{WW,2} = 0$ in (2.5)), thus, effectively, we enforce $\Pi = 0$. The resulting velocity p.d.f. is reported in figure 4, where we observe that, in fact, the inflectional regions disappear.

The p.d.f. of droplet accelerations, reported in figure 5, is Gaussian in the semi-dilute emulsion ($\phi = 38\%$) but, as the volume fraction is increased above $\phi_c = 64\%$, the p.d.f.s tend to develop fat (non-Gaussian) tails. A working fitting function is a stretched exponential of the type

$$P(\tilde{a}) = C \exp \left(- \frac{\tilde{a}^2}{\left(1 + \left(\frac{\beta|\tilde{a}|}{\sigma} \right)^\gamma \right) \sigma^2} \right), \quad (3.1)$$

where $\tilde{a} = a/a_{rms}$. The non-Gaussianity here, unlike turbulence, cannot be grounded on the complexity of the velocity field and of the associated multifractal distribution of the turbulent energy dissipation (Biferale *et al.* 2004). We are not facing, in fact, a fully developed turbulent flow and, moreover, the non-Gaussian signatures become evident on increasing the volume fraction above the jamming point ϕ_c , where the effective viscosity is higher (and, hence, the effective Reynolds number is lower). The origin of the non-Gaussianity is to be sought in the complex elastoplastic dynamics of the system, which is driven by long-range correlated irreversible stress relaxation events. Remarkably, in concentrated emulsions, it has been shown that the spatial distribution of stress drops in the

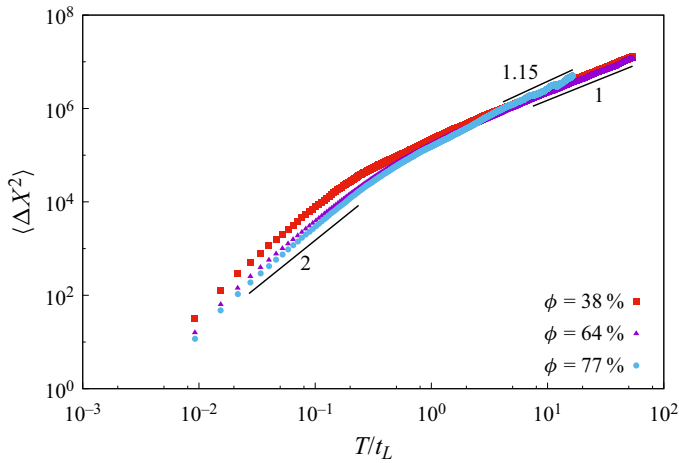


Figure 6. The MSD, $\langle \Delta X^2 \rangle$, for $\phi = 38\%$, 64% and 77% , in the forced regime. The MSD goes initially as T^2 , indicating a ballistic dynamics, followed by a diffusive growth, $T^{1/2}$, for $\phi < \phi_c$, whereas in the densely packed system ($\phi = 77\%$), there is a superdiffusive behaviour T^α , with $\alpha = 1.15$.

system displays a multifractal character (Kumar *et al.* 2020), which might be responsible for the statistical properties of the acceleration at high volume fraction, in formal analogy with the phenomenology of turbulence. The curves corresponding to (3.1) are reported in figure 5, for various values of the parameter γ , which gauges the deviations from the Gaussian form, and fixed $\beta = 0.35$ (obtained from best fitting) and $\sigma = 1$, the standard deviation of the Gaussian limit, such that, for $\gamma = 0$, the p.d.f. reduces to the normal distribution $\propto e^{-x^2/2}$. This is, indeed, the case for the lowest volume fraction, $\phi = 38\%$; the non-Gaussianity parameter γ then increases monotonically with ϕ up to $\gamma = 1.6$ for $\phi = 77\%$.

3.2. Dispersion: stirred regime

We focus now on the spatial dispersion of both single droplets as well as of droplet pairs. The single-droplet (or absolute) dispersion is defined in terms of the statistics of displacements, $\Delta X = X(t_0 + T) - X(t_0)$, where $X(t)$ is the position of the droplet centre of mass at time t ($t_0 = 1.25 \times 10^6$, let us recall, is the starting time of tracking). In figure 6 we show the mean square displacement (MSD), $\langle \Delta X^2 \rangle$, for volume fractions $\phi = 38\%$, 64% and 77% . Values are reported in logarithmic scale, with the time normalised (hereafter) by a characteristic large-scale time defined as $t_L = \sqrt{\rho_f L/A} \approx 38\,000$ (which is independent of the volume fraction), where A is the amplitude of the applied forcing (so A/ρ_f is an acceleration). In the diluted case, the MSD (figure 6) shows a cross-over at around $T \sim 5t_L$ between an initial ballistic motion, $\langle \Delta X^2 \rangle \sim T^2$, and a diffusive behaviour at later times, $\langle \Delta X^2 \rangle \sim T$. This is consistent with the typical Lagrangian dynamics of particles advected by chaotic and turbulent flows (Falkovich, Gawedzki & Vergassola 2001); for intermediate times, however, we observe a transitional region, in correspondence, approximately, with the cross-over, where the curve presents an inflection point with a locally super-ballistic slope. This is an interestingly non-trivial behaviour that certainly deserves further investigation. On increasing the volume fraction above ϕ_c the long-time growth seems to become steeper, although no clear conclusion can be reached

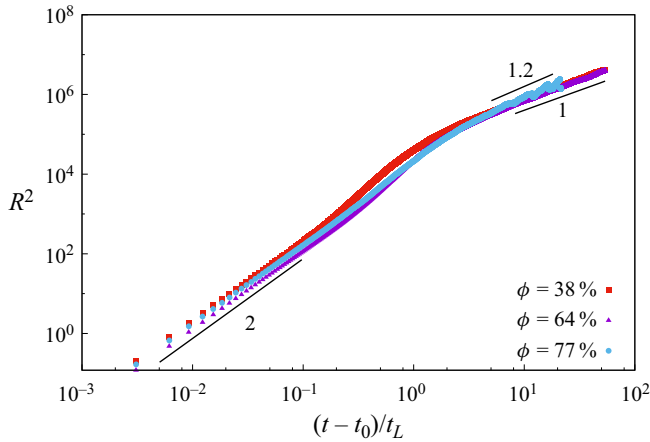


Figure 7. Mean square droplet pair separation $R^2(t) \equiv \langle |\mathbf{R}|^2 \rangle$ as a function of time for volume fractions $\phi = 38\%$, 64% , 77% . The power laws are reported as solid lines, evidencing a slight deviation from the diffusive regime for the most concentrated case.

due to the extremely small range available in the numerical simulation. A deeper insight into the small-scale dynamics can be grasped by looking at the pair dispersion, namely the statistics of separations

$$\mathbf{R}_{ij}(t) = \mathbf{X}_i(t) - \mathbf{X}_j(t), \tag{3.2}$$

at time t for all pairs of droplets i, j that are nearest neighbours (i.e. such that their corresponding cells in a Voronoi tessellation of the centre of mass distribution are in contact) at $t = t_0$. The observable in (3.2) is, in fact, insensitive to contamination from mean homogeneous large-scale flows, if present. In figure 7 we report the mean square value $R^2(t) \equiv \langle |\mathbf{R}_{ij}|^2 \rangle_{\{ij\}}$ (where the average is over the initially neighbouring pairs) as a function of time, for $\phi = 38\%$, 64% and 77% . Analogously to the MSD, $R^2(t)$ grows in time and, after an initial ballistic transient, it follows a diffusive-like behaviour. Again, for $\phi > \phi_c$, one may argue about a superdiffusive behaviour.

3.3. Velocity and acceleration statistics: ageing regime

When the large-scale forcing is switched off, in diluted conditions (below the close packing volume fraction), the system relaxes via a long transient, where the kinetic energy decays to zero. Instead, at high volume fraction (in the jammed phase), the emulsion is never completely at rest, due to diffusion and droplet elasticity favouring the occurrence of plastic events, namely, the local topological rearrangement of a few droplets (i.e. during the ‘ageing’ of the material). Therefore, we consider here only the latter situation and focus on the case $\phi = 77\%$; hereafter, we present data obtained with forcing amplitude $A = 4.05 \times 10^{-7}$ (see the ϕ_6 row in table 1), which yielded a larger number of droplets ($\sim 10^3$) in the steady state, which improved the statistics. The p.d.f. of the droplet velocities is reported in figure 8. Since there is no mean flow, the p.d.f. is an even function of its argument. We show, therefore, the distribution of the absolute values in logarithmic scale, in order to highlight the power-law behaviour v^{-3} . Interestingly, the p.d.f. of acceleration also develops a power-law tail $P(a) \sim a^{-3}$ (the p.d.f.s for velocity and acceleration do, in fact, overlap, upon rescaling by the respective standard deviations, see figure 8), reflecting the fact that, when stirring is switched off, the high effective viscosity overdamps the

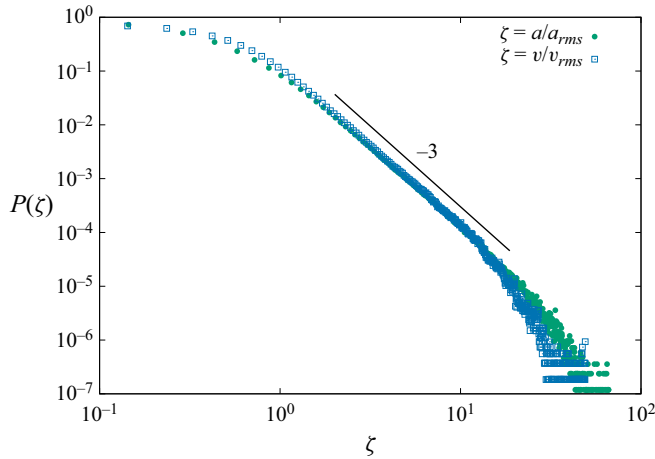


Figure 8. The p.d.f.s of the absolute values of droplet velocities and accelerations, rescaled by their own r.m.s. values (given in table 1), in the ageing regime. Both p.d.f.s show a power-law, $P(\zeta) \sim \zeta^{-3}$, decay.

dynamics, thus enslaving the acceleration to the velocity (by Stokesian drag), $a \sim u/\tau_s$ (assuming the Stokes time is equal for all droplets, which is reasonable given the very low spread of size distribution in the ageing regime Girotto *et al.* 2022).

3.4. Dispersion: ageing regime

In the ageing regime at the largest volume fraction, $\phi = 77\%$, the MSD goes as $\langle \Delta X^2 \rangle \sim T^2$ for short times, signalling a ballistic regime, followed by a super-diffusive regime $\langle \Delta X^2 \rangle \sim T^{3/2}$ (see inset of figure 9). The short-time ballistic regime is consistent with a theoretical prediction based on the superposition of randomly distributed elastic dipoles (following structural micro-collapses) (Bouchaud & Pitard 2001) and with results from experiments with colloidal gels (Cipelletti *et al.* 2000) and foams (Giavazzi *et al.* 2021). The scaling $\langle \Delta X^2 \rangle \sim T^{3/2}$ is, instead, slightly steeper than the experimentally measured $\sim T^{1.2}$ (Giavazzi *et al.* 2021).

The ballistic regime $\langle \Delta X^2 \rangle \sim T^2$ entails a power-law tail of the p.d.f. of separations for short times, $P(\Delta X) \sim \Delta X^{-3}$, corresponding to the self-part of the van Hove distribution (Hansen & McDonald 1986), as reported in figure 9 (Cipelletti *et al.* 2003; Giavazzi *et al.* 2021). This observation finds correspondence, as one could expect, in the p.d.f. of the droplet velocities, shown in figure 8.

The study of pair dispersion, reported in figure 10, evidences, for the mean square pair separation (in the inset), a ballistic regime, $\langle R^2 \rangle \sim t^2$, followed by a superdiffusive behaviour, $\langle R^2 \rangle \sim t^{4/3}$. The persistence of ballistic motion is expected to match the decorrelation of trajectories following a plastic event, therefore the cross-over time, t_c , can be approximately estimated as the time taken by a droplet to travel the typical size of a rearrangement, $\xi \approx 2d$ (which is an intrinsic scale for correlation lengths in soft glassy materials Goyon *et al.* 2008; Dollet *et al.* 2015); since the characteristic velocity is $v_c \sim \Gamma/6\eta$ (see figure 4 and discussion thereof), we get $t_c \sim 12d\eta/\Gamma \approx 7 \times 10^3$, indicated in the inset of figure 10 with a dashed line.

By analogy with Richardson's description of turbulent diffusion (Richardson 1926; Falkovich *et al.* 2001; Boffetta & Sokolov 2002), we propose a phenomenological approach to derive the full pair separation p.d.f. in the superdiffusive regime. We assume that

Lagrangian statistics of concentrated emulsions

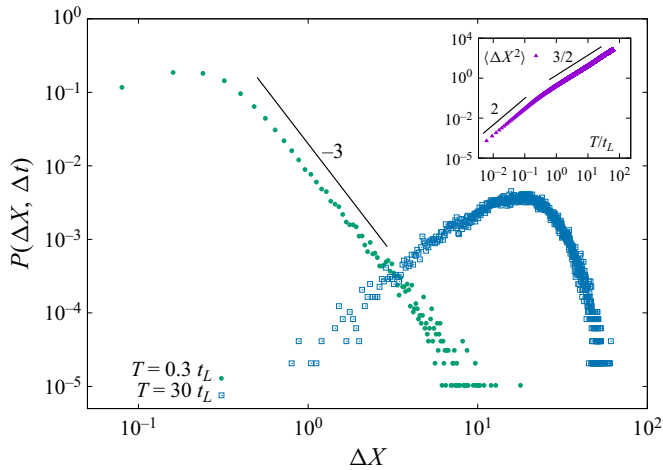


Figure 9. Absolute dispersion of droplets in the ageing regime at $\phi = 77\%$. (Main panel) The p.d.f.s of droplet displacements (van Hove functions) at two time increments T , in the ageing regime; for the time increment in the ballistic regime the p.d.f. shows, as expected, a ΔX^{-3} decay, consistent with the velocity p.d.f., figure 8. (Inset) Mean square displacement, $\langle \Delta X^2 \rangle$, vs time increment; the solid lines highlight the ballistic and superdiffusive behaviours.

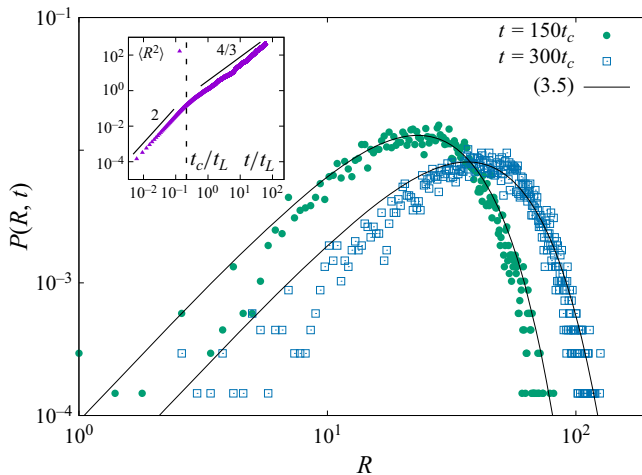


Figure 10. (Main panel) The p.d.f.s of the pair separations, $P(R, t)$ at two instants of time in the super-diffusive regime, $t_{1,2} > t_c$; the solid lines are the theoretical prediction, (3.5), with parameters $\mathcal{A} = 1.7$, $c = 6 \times 10^{-4} < d < 3/2 t_c^{-1}$. (Inset) Mean square separation as a function of time: a ballistic regime, $\langle R^2 \rangle \sim t^2$, is followed by a super-diffusive one, $\langle R^2 \rangle \sim t^{4/3}$, the cross-over between the two regimes occurring around $t \approx t_c = 12d\eta/\gamma$, indicated with the dashed line.

the p.d.f. evolves according to a generalised diffusion equation, with a scale-dependent effective diffusivity, D_{eff} which, dimensionally, should be proportional to $d\langle R^2 \rangle/dt$. Since $\langle R^2 \rangle \sim t^{4/3}$ (and, consequently, $t \sim R^{3/2}$), we have

$$D_{eff} \propto \frac{d\langle R^2 \rangle}{dt} \sim t^{1/3} \Rightarrow D_{eff} \propto R^{1/2} \equiv cR^{1/2}. \quad (3.3)$$

The diffusion equation thus reads

$$\partial_t P(R, t) = \partial_R \left(cR^{1/2} \partial_R P(R, t) \right), \quad (3.4)$$

that admits as solution (with the condition of unit area at all times) the following non-Gaussian distribution:

$$P(R, t) = \mathcal{A} \frac{2R^2}{27c^2 t^2} \exp \left(-\frac{4R^{3/2}}{9ct} \right). \quad (3.5)$$

The p.d.f.s of pair separations measured at two instants of time in the superdiffusive regime, $t_1 \approx 150t_c$ and $t_2 \approx 300t_c$, are shown in figure 10 together with the prediction of (3.5), with fitting parameter $c = 6 \times 10^{-4} \langle d \rangle^{3/2} t_c^{-1}$, plotted as solid lines. The agreement obtained between theory and numerics is quite remarkable.

4. Conclusions

In this paper, using 3-D numerical simulations, we discussed the complex statistical and dynamical properties of concentrated emulsions. The simulations were carried out using a recently developed procedure for *in silico* emulsification (Giroto *et al.* 2022) which is based on the modelling of stabilised binary immiscible liquid mixtures with high volume fractions of the dispersed phase. We also developed a novel tracking algorithm that allowed us to study the emulsion physics at the droplet-resolved scale from a Lagrangian viewpoint, across various concentrations, from the semi-dilute to the jammed regimes.

Using the same large-scale forcing, we studied the mean rates of droplet breakup $\bar{\beta}$ and coalescence $\bar{\kappa}$, the droplet velocity, acceleration and dispersions. We have shown that $\bar{\beta}$, $\bar{\kappa}$ and the average droplet diameter $\langle d \rangle$ show a divergent-like behaviour for ϕ close to the catastrophic phase inversion ϕ_{cpi} .

Also, we highlighted how the elastic properties and the plastic microdynamics of densely packed ensembles of droplets in close contact are responsible of the non-Gaussian character of the droplet acceleration and, more moderately, of the velocity statistics.

We further investigated the single-droplet diffusion in terms of both the MSD and the self-part of the van Hove distribution functions. In particular, for a rather large value of ϕ , we stopped the large-scale forcing and we studied the so-called aging regime. We observe a well-defined cross-over in time from ballistic to super-diffusive behaviour, in agreement with previous theoretical and experimental results. Further investigations will focus on the dispersion properties on larger systems and for longer observation times, as well as on the relation of the Lagrangian properties of the droplets to the stress distribution throughout the system. In perspective, we foresee extending of the reach of the present work to extreme conditions of volume fractions and forcing amplitudes, whereby the emulsion tends to lose stability and to undergo a catastrophic phase inversion. In this limit, too, the Lagrangian approach is of invaluable utility. Overall, our approach suggested a bridge between classical tools for Lagrangian high Reynolds number flows and complex fluid rheology, which paves the way to the inspection of unexplored aspects of the physics of soft materials.

Acknowledgements. We are thankful to C. Sun and L. Yi for useful discussions and P. Perlekar for a fruitful interaction at the initial stage of the work.

Funding. Numerical simulations were performed thanks to granted PRACE projects (ID: 2018184340 and 2019204899) along with CINECA and BSC for access to their HPC systems. This work was partially sponsored by NWO domain Science for the use of supercomputer facilities.

Declaration of interests. The authors report no conflict of interest.

Author ORCIDs.

 Andrea Scagliarini <https://orcid.org/0000-0002-3893-746X>;

 Federico Toschi <https://orcid.org/0000-0001-5935-2332>.

REFERENCES

- BELARDINELLI, D. & SBRAGAGLIA, M. 2013 Interaction pressure tensor for a class of multicomponent lattice Boltzmann models. *Phys. Rev. E* **88**, 013306.
- BENZI, R., BERNASCHI, M., SBRAGAGLIA, M. & SUCCI, S. 2010 Herschel–Bulkley rheology from lattice kinetic theory of soft glassy materials. *Europhys. Lett.* **91** (1), 14003.
- BENZI, R., SBRAGAGLIA, M., PERLEKAR, P., BERNASCHI, M., SUCCI, S. & TOSCHI, F. 2014 Direct evidence of plastic events and dynamic heterogeneities in soft-glasses. *Soft Matt.* **10**, 4615–4624.
- BENZI, R., SBRAGAGLIA, M., SUCCI, S., BERNASCHI, M. & CHIBBARO, S. 2009 Mesoscopic lattice Boltzmann modeling of soft-glassy systems: theory and simulations. *J. Chem. Phys.* **131** (10), 104903.
- BENZI, R., SUCCI, S. & VERGASSOLA, M. 1992 The lattice boltzmann equation: theory and applications. *Phys. Rep.* **222** (3), 145–197.
- BERGERON, V. 1999 Forces and structure in thin liquid soap films. *J. Phys.: Condens. Matter* **11**, R215.
- BIFERALE, L., BOFFETTA, G., CELANI, A., DEVENISH, B.J., LANOTTE, A. & TOSCHI, F. 2004 Multifractal statistics of Lagrangian velocity and acceleration in turbulence. *Phys. Rev. Lett.* **93**, 064502.
- BIFERALE, L., PERLEKAR, P., SBRAGAGLIA, M., SRIVASTAVA, S. & TOSCHI, F. 2011 A lattice Boltzmann method for turbulent emulsions. *J. Phys.: Conf. Ser.* **318** (5), 052017.
- BOCQUET, L., COLIN, A. & AJDARI, A. 2009 Kinetic theory of plastic flow in soft glassy materials. *Phys. Rev. Lett.* **103**, 036001.
- BOFFETTA, G. & SOKOLOV, I.M. 2002 Relative dispersion in fully developed turbulence: the Richardson’s law and intermittency corrections. *Phys. Rev. Lett.* **88**, 094501.
- BONN, D., DENN, M.M., BERTHIER, L., DIVOUX, T. & MANNEVILLE, S. 2017 Yield stress materials in soft condensed matter. *Rev. Mod. Phys.* **89**, 035005.
- BOUCHAMA, F., VAN AKEN, G.A., AUTIN, A.J.E. & KOPER, G.J.M. 2003 On the mechanism of catastrophic phase inversion in emulsions. *Colloids Surf. (A)* **231**, 11–17.
- BOUCHAUD, J.-P. & PITARD, E. 2001 Anomalous dynamical light scattering in soft glassy gels. *Eur. Phys. J. E* **6**, 231–236.
- BOUZID, M., IZZET, A., TRULSSON, M., CLÉMENT, E., CALUDIN, P. & ANDREOTTI, B. 2015 Non-local rheology in dense granular flows: revisiting the concept of fluidity. *Eur. Phys. J. E* **38**, 125.
- BRANDT, L. & COLETTI, F. 2022 Particle-laden turbulence: progress and perspectives. *Annu. Rev. Fluid Mech.* **54**, 159–189.
- CERBINO, R. & TRAPPE, V. 2008 Differential dynamic microscopy: probing wave vector dependent dynamics with a microscope. *Phys. Rev. Lett.* **100**, 188102.
- CHAN, W.H.R., DODD, M.S., JOHNSON, P.L. & MOIN, P. 2021 Identifying and tracking bubbles and drops in simulations: a toolbox for obtaining sizes, lineages, and breakup and coalescence statistics. *J. Comput. Phys.* **432**, 110156.
- CHIARELLO, E., GUPTA, A., MISTURA, G., SBRAGAGLIA, M. & PIERNO, M. 2017 Droplet breakup driven by shear thinning solutions in a microfluidic T-junction. *Phys. Rev. Fluids* **2**, 123602.
- CIPELLETTI, L., MANLEY, S., BALL, R.C. & WEITZ, D.A. 2000 Universal aging features in the restructuring of fractal colloidal gels. *Phys. Rev. Lett.* **84**, 2275–2278.
- CIPELLETTI, L. & RAMOS, L. 2005 Slow dynamics in glassy soft matter. *J. Phys.: Condens. Matter* **17**, R253.
- CIPELLETTI, L., RAMOS, L., MANLEY, S., PITARD, E., WEITZ, D.A., PASHKOVSKI, E.E. & JOHANSSON, M. 2003 Universal non-diffusive slow dynamics in aging soft matter. *Faraday Discuss.* **123**, 237–251.
- COHEN-ADDAD, S., HOHLER, R. & PITOIS, O. 2013 Flow in foams and flowing foams. *Annu. Rev. Fluid Mech.* **45**, 241.
- COUSSOT, P. 2005 *Rheometry of Pastes, Suspensions, and Granular Materials: Applications in Industry and Environment*. Wiley.
- DERJAGUIN, B.V. & CHURAEV, N.V. 1978 On the question of determining the concept of disjoining pressure and its role in the equilibrium and flow of thin films. *J. Colloid Interface Sci.* **66**, 389–398.
- DIJKSMAN, J.A. 2019 Connecting the drops: observing collective flow behavior in emulsions. *Front. Phys.* **7**, 198.
- DOLLET, B. & CHRISTOPHE, R. 2014 Rheology of aqueous foams. *C. R. Phys.* **15**, 731.

- DOLLET, B., SCAGLIARINI, A. & SBRAGAGLIA, M. 2015 Two-dimensional plastic flow of foams and emulsions in a channel: experiments and lattice Boltzmann simulations. *J. Fluid Mech.* **766**, 556–589.
- DURIAN, D.J. 1995 Foam mechanics at the bubble scale. *Phys. Rev. Lett.* **75**, 4780–4783.
- DURIAN, D.J., WEITZ, D.A. & PINE, D.J. 1991 Multiple light-scattering probes of foam structure and dynamics. *Science* **252**, 686–688.
- FALKOVICH, G., GAWEDZKI, K. & VERGASSOLA, M. 2001 Particles and fields in fluid turbulence. *Rev. Mod. Phys.* **73**, 913–975.
- FEI, L., SCAGLIARINI, A., LUO, K.H. & SUCCI, S. 2020 Discrete fluidization of dense monodisperse emulsions in neutral wetting microchannels. *Soft Matt.* **16**, 651–658.
- FRIJTERS, S., KRÜGER, T. & HARTING, J. 2015 Parallelised Hoshen–Kopelman algorithm for lattice-Boltzmann simulations. *Comput. Phys. Commun.* **189**, 92–98.
- GAO, Q., DEANE, G.B., LIU, H. & SHEN, L. 2021 A robust and accurate technique for Lagrangian tracking of bubbles and detecting fragmentation and coalescence. *Intl J. Multiphase Flow* **135**, 103523.
- GAYLO, D.B., HENDRICKSON, K. & YUE, D.K.P. 2022 An Eulerian label advection method for conservative volume-based tracking of bubbles/droplets. *J. Comput. Phys.* **470** (C), 111560.
- GIAVAZZI, F., TRAPPE, V. & CERBINO, R. 2021 Multiple dynamic regimes in a coarsening foam. *J. Phys.: Condens. Matter* **33**, 024002.
- GIOTTO, I., BENZI, R., DI STASO, G., SCAGLIARINI, A., SCHIFANO, F.M. & TOSCHI, F. 2022 Build up of yield stress fluids via chaotic emulsification. *J. Turbul.* **23**, 265–275.
- GOYON, J., COLIN, A., OVARLEZ, G., AJDARI, A. & BOCQUET, L. 2008 Spatial cooperativity in soft glassy flows. *Nature* **454**, 84–87.
- GUPTA, A. & SBRAGAGLIA, M. 2016 Effects of viscoelasticity on droplet dynamics and break-up in microfluidic T-junctions: a lattice Boltzmann study. *Eur. Phys. J. E* **39**, 6.
- GUPTA, A., SBRAGAGLIA, M., BELARDINELLI, D. & SUGIYAMA, K. 2016 Lattice Boltzmann simulations of droplet formation in confined channels with thermocapillary flows. *Phys. Rev. E* **94**, 063302.
- GUPTA, A., SBRAGAGLIA, M. & SCAGLIARINI, A. 2015 Hybrid lattice Boltzmann/finite difference simulations of viscoelastic multicomponent flows in confined geometries. *J. Comput. Phys.* **291**, 177–197.
- HANSEN, J.-P. & McDONALD, I.R. 1986 *Theory of Simple Liquids*. Academic.
- HE, L., REN, X., GAO, Q., ZHAO, X., YAO, B. & CHAO, Y. 2017 The connected-component labeling problem: a review of state-of-the-art algorithms. *Pattern Recognit.* **70**, 25–43.
- HENDRICKSON, K., WEYMOUTH, G.D. & YUE, D.K.-P. 2020 Informed component label algorithm for robust identification of connected components with volume-of-fluid method. *Comput. Fluids* **197**, 104373.
- HERRMANN, M. 2010 A parallel Eulerian interface tracking/Lagrangian point particle multi-scale coupling procedure. *J. Comput. Phys.* **229** (3), 745–759.
- HOSHEN, J. & KOPELMAN, R. 1976 Percolation and cluster distribution. I. Cluster multiple labeling technique and critical concentration algorithm. *Phys. Rev. B* **14**, 3438–3445.
- KRÜGER, T., KUSUMAATMAJA, H., KUZMIN, A., SHARDT, O., SILVA, G. & VIGGEN, E.M. 2016 *The Lattice Boltzmann Method: Principles and Practice*. Springer.
- KUMAR, P., KORKOLIS, E., BENZI, R., DENISOV, D., NIEMEIJER, A., SCHALL, P., TOSCHI, F. & TRAMPERT, J. 2020 On interevent time distributions of avalanche dynamics. *Sci. Rep.* **10**, 626.
- LARSON, R.G. 1999 *The Structure and Rheology of Complex Fluids*. Oxford University Press.
- LI, Q., PENG, X. & MCKENNA, G.B. 2019 Physical aging and compressed exponential behaviors in a model soft colloidal system. *Soft Matt.* **15**, 2336–2347.
- LOWENBERG, M. & HINCH, E.J. 1996 Numerical simulation of a concentrated emulsion in shear flow. *J. Fluid Mech.* **321**, 395–419.
- MASON, T.G., GANESAN, K., VAN ZANTEN, J.H., WIRTZ, D. & KUO, S.C. 1997 Particle tracking microrheology of complex fluids. *Phys. Rev. Lett.* **79**, 3282–3285.
- MASON, T.G. & WEITZ, D.A. 1995 Optical measurements of frequency-dependent linear viscoelastic moduli of complex fluids. *Phys. Rev. Lett.* **74**, 1250–1253.
- MCCLEMENTS, D.J. 2015 *Food Emulsions: Principles, Practices and Techniques*. CRC.
- PERAZZO, A., PREZIOSI, V. & GUIDO, S. 2015 Phase inversion emulsification: current understanding and applications. *Adv. Colloid Interface Sci.* **222**, 581–599.
- PERLEKAR, P., BENZI, R., CLERCX, H.J.H., NELSON, D.R. & TOSCHI, F. 2014 Spinodal decomposition in homogeneous and isotropic turbulence. *Phys. Rev. Lett.* **112**, 014502.
- PERLEKAR, P., BIFERALE, L., SBRAGAGLIA, M., SRIVASTAVA, S. & TOSCHI, F. 2012 Droplet size distribution in homogeneous isotropic turbulence. *Phys. Fluids* **24** (6), 065101.
- RAMOS, L. & CIPELLETTI, L. 2001 Ultraslow dynamics and stress relaxation in the aging of a soft glassy system. *Phys. Rev. Lett.* **87**, 245503.

Lagrangian statistics of concentrated emulsions

- RICHARDSON, L.F. 1926 Atmospheric diffusion shown on a distance-neighbour graph. *Proc. R. Soc. Lond. A* **110**, 709–737.
- ROWLINSON, J.S. & WIDOM, B. 2002 *Molecular Theory of Capillarity*. Dover.
- RUZICKA, B., ZULIAN, L. & RUOCCO, G. 2004 Routes to gelation in a clay suspension. *Phys. Rev. Lett.* **93**, 258301.
- SBRAGAGLIA, M., BENZI, R., BERNASCHI, M. & SUCCI, S. 2012 The emergence of supramolecular forces from lattice kinetic models of non-ideal fluids: applications to the rheology of soft glassy materials. *Soft Matt.* **8**, 10773–10782.
- SHAN, X. & CHEN, H. 1993 Lattice Boltzmann model for simulating flows with multiple phases and components. *Phys. Rev. E* **47**, 1815–1819.
- SHAN, X. & CHEN, H. 1994 Simulation of nonideal gases and liquid-gas phase transitions by the lattice Boltzmann equation. *Phys. Rev. E* **49**, 2941–2948.
- SQUIRES, T.M. & MASON, T.G. 2010 Fluid mechanics of microrheology. *Annu. Rev. Fluid Mech.* **42**, 413–428.
- SUCCI, S. 2018 *The Lattice Boltzmann Equation for Complex States of Flowing Matter*. Oxford University Press.
- TCHOLAKOVA, S., VANKOVA, N., DENKOV, N.D. & DANNER, T. 2007 Emulsification in turbulent flow: 3. Daughter drop-size distribution. *J. Colloid Interface Sci.* **310**, 570–589.
- TORQUATO, S. & STILLINGER, F.H. 2010 Jammed hard-particle packings: from Kepler to Bernal and beyond. *Rev. Mod. Phys.* **82**, 2633–2672.
- TOSCHI, F. & BODENSCHATZ, E. 2009 Lagrangian properties of particles in turbulence. *Annu. Rev. Fluid Mech.* **41**, 375–404.
- VANKOVA, N., TCHOLAKOVA, S., DENKOV, N.D., IVANOV, I.B., VULCHEV, V.D. & DANNER, T. 2007a Emulsification in turbulent flow: 1. Mean and maximum drop diameters in inertial and viscous regimes. *J. Colloid Interface Sci.* **312**, 363–380.
- VANKOVA, N., TCHOLAKOVA, S., DENKOV, N.D., VULCHEV, V.D. & DANNER, T. 2007b Emulsification in turbulent flow: 2. Breakage rate constants. *J. Colloid Interface Sci.* **313**, 612–629.
- VARAGNOLO, S., MISTURA, G., PIERNO, M. & SBRAGAGLIA, M. 2015 Sliding droplets of xanthan solutions: a joint experimental and numerical study. *Eur. Phys. J. E* **38**, 126.